STRUCTURAL CONTROL AND HEALTH MONITORING
Struct. Control Health Monit. 2016; **23**:1417–1441
Published online 15 February 2016 in Wiley Online Library (wileyonlinelibrary.com). DOI: 10.1002/stc.1839

Aeroelastic control of long-span suspension bridges with controllable winglets

Konstantinos Nikolaos Bakis*,†, Matteo Massaro, Martin S. Williams and David J. N. Limebeer

Department of Engineering Science, University of Oxford, Oxford, UK

SUMMARY

The structural-aerodynamic modelling and dynamic stabilization of a three-dimensional suspension bridge model is considered. Our emphasis is on investigating the effectiveness of leading and trailing edge flaps in suppressing aeroelastic instabilities. The East Great Belt Bridge is chosen as a design example, and its aeroelastic limits are computed using both thin aerofoil theory and flutter derivatives. The problem is cast in an efficient reduced size finite element formulation with aerodynamic forces expressed in the Laplace domain by use of a high-fidelity rational function approximation. Circulatory aerodynamic forces are modelled using a feedback loop for every element, and the problem is expressed in a form suitable for implementation of modern control techniques. The structure's full multimodal response is considered, and numerical predictions show very good agreement against experimental data from the literature. In order to account for modelling errors and uncertainties while designing the controller, elements from robust control theory are invoked. The stability and robustness of the bridge when fitted with flaps controlled by optimal and suboptimal H_∞ controllers are discussed for varying lengths of control surfaces along the suspended span as the optimum configuration for aerodynamic performance is investigated.

Received 2 June 2015; Revised 7 November 2015; Accepted 24 December 2015

KEY WORDS: long-span bridges; thin aerofoil theory; flutter; torsional divergence; passive aerodynamic control; erection stage; robust control; flaps; Humber bridge

1. INTRODUCTION

It is well understood that aeroelastic instabilities like flutter and torsional divergence pose limits to the length increase of cable-supported bridges, with the now iconic Tacoma Narrows bridge disaster serving as a reminder of the importance of efficient aerodynamic design. Increasing span lengths pose a challenge to aeroelastic stability, and experience gained from record span projects such as the Akashi Kaikyo Bridge [1] and Great Belt East Bridge showed that classic aerodynamic design either in the form of deep truss girders (Akashi Bridge) or the more modern flat box girder solution (Humber, Bosporus, Great Belt) reaches its limit for spans approaching 2000 m [2]. To overcome these limitations, appropriate countermeasures should be adopted [3], which traditionally have focused on the deck's aerodynamic improvement or alternatively on the implementation of active and passive control methodologies.

Control applications to civil engineering structures have been gaining in popularity, thanks to novel advances in the field [4], with a particular emphasis to bridge structures [5]. Control of flutter instability by active control surfaces was first proposed by Ostenfeld and Larsen in [6]. The premise is that rotational movement of control surfaces adjacent to the deck generates aerodynamic forces that aim at stabilizing deck movement. Further analysis was later undertaken by Wilde and Fujino [7,8], where flaps were

*Correspondence to: Konstantinos Nikolaos Bakis, Department of Engineering Science, University of Oxford, Oxford, UK.
†E-mail: konstantinos-nikolaos.bakis@new.ox.ac.uk

implemented on a deck segment. A rational function approximation (RFA) was used to model the unsteadiness of the flow in the time-domain, and a variable gain output feedback controller was implemented. Omenzetter *et al.* [9,10] extended the flap configuration, taking into account the three-dimensionality of the bridge, and a pure-gain passive mechanism was proposed. Passive pure-gain controllers are in principle easy to implement, but these systems forego the advantages that might accrue from phase compensation. Fixed-phase controllers, such as those derived in [11], are difficult to construct physically. Realizable systems that introduce frequency-dependent phase may operate satisfactorily, but this has not thus far been established using a full bridge model. More recently, Li [12] performed an active control procedure using a pair of rotatable winglets at a distance from the deck. The feasibility of a passive control mechanism against flutter instability during erection of a suspension bridge has been investigated in [13], whereas some efforts have been made to combine the advantages of control surfaces with a tuned mass damper [14,15], although a detailed analysis has not been reported yet. Up to date, there has been no practical application of implementing actively or passively controlled flaps to a bridge because their reliability and effectiveness have not been clearly demonstrated.

In terms of the aerodynamic control of bridge structures, three-dimensional aeroelastic modelling by expressing unsteady aerodynamic forces in the frequency domain has been reported in [16–18]. The procedure involves algorithms such as the k-method and the p-k method inherited from the aeronautics industry, which are based on an iterative procedure for both the wind velocity and the frequency of the oscillating forces. A state–space approach that fits the unsteady part of the aerodynamic forces by use of rational function approximations [19] makes however the iterative process redundant. An implementation of this procedure to a full bridge structure has been presented by Omenzetter *et al.* [9] and Chen *et al.* [20] for thin aerofoil and flutter derivatives, respectively.

This work extends previous analytic investigations [21,22] of a deck-flap system into a three-dimensional bridge model having flaps of finite length along the main span. The emphasis in this paper is placed on active control schemes, which enables the determination of the minimum surfaces needed for aeroelastic control. In our work, we build a high-fidelity rational approximation of the classical Theodorsen circulation function, which is used for every element of the bridge structure. The structural part of this work is based on Abdel Ghaffar's finite element (FE) formulation [23–25], which is appropriately modified to account for a streamlined box girder (while the original formulation dealt with a truss girder). Forces on cables are computed by solving the nonlinear cable equation [26]. We validate the model by simulating the modal characteristics of the Great Belt Bridge and comparing them with previous studies. We later formulate the aeroelastic FE model by employing thin aerofoil theory [27] as well as expressing the aerodynamic loading through experimentally derived flutter derivatives [28]. For the first case, a high-fidelity quartic rational approximation of Theodorsen's circulation function is considered, and for the second case, Roger's [29] approximation is used. Results show that the thin aerofoil assumption is very effective in predicting flutter instability limits for a flat box girder like the one herein considered. The aforementioned analyses also expose a non-oscillatory instability referred to as torsional divergence. The torsional divergence mode is an aerodynamic mode that goes unstable when there is a loss of torsional rigidity because of cancellation of the (positive) torsional stiffness of the structure by the negative pitch-related aerodynamic moment [30].

This paper places emphasis on formulating the full multimodal aeroelastic response by means of a reduced size model. A very good agreement in terms of modal responses is obtained with only 350 structural degrees of freedom. By using feedback for the unsteady circulatory component of the aerodynamics, we reduce the number of aerodynamic states to half. For the case of the Great Belt (GB) cross section, thin aerofoil theory and flutter derivatives give very close predictions to flutter onset, thus corroborating the justification of the wing–aileron–tab transformation for modelling the flap aerodynamic contribution. Previous work including bridge stabilization with controllable surfaces either uses passive systems, which have the advantage of not requiring power source but use a simplistic control approach neglecting phase compensation and robustness properties, or make use of active control techniques, optimal control and pole placement algorithm, which again neglect robustness issues. This work aims to optimize the closed-loop system's robustness to uncertainties, which can be interpreted as uncertainty in modal characteristics or aerodynamic parameters. Our goal is to establish an active control strategy that results in a minimum area of control surfaces along the span while

DOI: 10.1002/stc

attaining good robustness characteristics (Figure 1). In conclusion, it is shown that for wind speeds above the divergence speed, there is a clear loss in uncertainty tolerance, and in conclusion, we demonstrate the effectiveness of the designed controllers by simulating the response in the time domain. The analysis presented in this paper is of an analytical nature and concentrates on the control design process on a full FE bridge model. Experimental work is carried through in conjunction to this work [31] to validate the numerical assumptions.

2. STRUCTURAL MODEL

This section provides a procedure overview for constructing a full bridge model according to Abdel Ghaffar's structural framework [23–25] and compares the results with previous analyses of the Great Belt Bridge. The FE framework adopted provides a significant reduction of the computational burden because it accounts for the effect of the main cables and hangers for every deck element indirectly. The motion of long-span bridges in the vertical, lateral and torsional direction can with a high degree of accuracy be considered independent from one another, so each case was treated separately and no coupling between them was assumed. In the pure vertical modes, all points of a given cross section move the same amount and remain in phase. In the torsional case, the bridge section rotates about its centre point, and for the lateral motion, each cross section swings in a pendular fashion in its own vertical plane, and therefore, there is an incidental upward movement of the cables and of the suspended structure.

2.1. Modelling methodology

Figure 2a presents the degrees of freedom, vertical translation and rotation, corresponding to the vertical vibration case. Because the displacements of each stiffening structure node must equal the displacements of the corresponding cable node, it is appropriate to define only the nodes on the centre line of the deck element. Similar element configurations are defined for the lateral and torsional vibration cases. The general procedure for deriving the stiffness and mass matrices for a typical deck element consists firstly in expressing the potential and kinetic energy of the suspended structure and the cables separately for each vibration case. In order to formulate the FE approach, the Hermitian cubic polynomials are chosen to build the shape functions of the element, expressing the vertical v, lateral l and torsional t displacements at every internal point as a function of the nodal displacements $q_{1..12}$:

$$\begin{Bmatrix} v(x) \\ l(x) \\ t(x) \end{Bmatrix} = \begin{bmatrix} H_1 & H_2 & 0 & 0 & 0 & 0 & H_3 & H_4 & 0 & 0 & 0 & 0 \\ 0 & 0 & H_1 & H_2 & 0 & 0 & 0 & 0 & H_3 & H_4 & 0 & 0 \\ 0 & 0 & 0 & 0 & 0 & H_5 & 0 & 0 & 0 & 0 & 0 & H_6 \end{bmatrix} \begin{Bmatrix} q_1 \\ \vdots \\ q_{12} \end{Bmatrix} \quad (1)$$

where

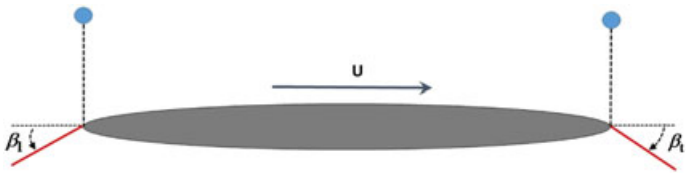

Figure 1. Cross section of a streamlined long-span suspension bridge with flutter suppression controllable flaps. The wind speed is denoted as U, while the leading-edge and trailing-edge flap angle are denoted as β_l and β_t, respectively.

DOI: 10.1002/stc

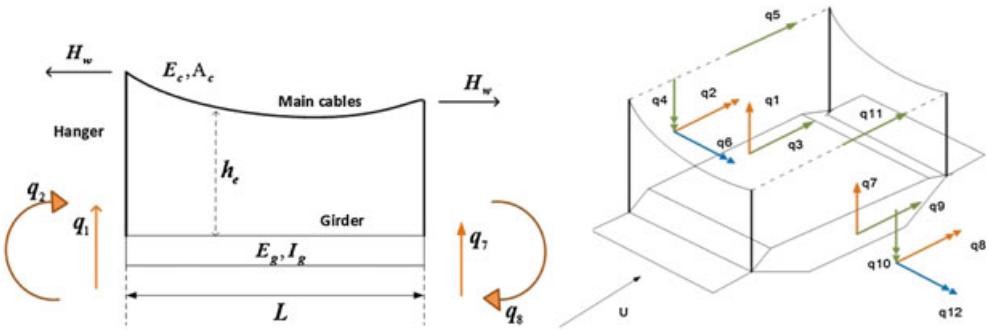

(a) (b)

Figure 2. (a) Nodal degrees of freedom of the FE element for the vertical vibration case and (b) all degrees of freedom of the FE element (orange q_1, q_2, q_7, q_8 correspond to the vertical, green q_3, q_4, q_5, q_9, q_{10}, q_{11} to the lateral and blue q_6, q_{12} to the torsional degrees of freedom).

$$H_1(x) = 1 - 3\frac{x^2}{L^2} + 2\frac{x^3}{L^3} \quad H_2(x) = -\left(x - 2\frac{x^2}{L} + \frac{x^3}{L^2}\right)$$
$$H_3(x) = 3\frac{x^2}{L^2} - 2\frac{x^3}{L^3} \quad H_4(x) = -\left(-\frac{x^2}{L} + \frac{x^3}{L^2}\right) \tag{2}$$
$$H_5(x) = 1 - \frac{x}{L} \quad H_6(x) = \frac{x}{L}$$

with $0 < x < L$ the position along the element spanwise length.

The combination of all three vibration components (vertical *v*, lateral *l* and torsional *t*) culminates in an element having six degrees of freedom per node as illustrated in Figure 2b.

Implementing Equation (1) in the potential and kinetic energy expressions yields the elemental mass matrices and elemental stiffness matrices expressing the elastic stiffness of the girder and the gravity stiffness of the cables, as well as a distributed matrix expressing the elastic stiffness of the cables. The gravity stiffness matrix is related to the energy stored in the cable because of the constant horizontal force. The elastic stiffness on the other hand stems from the additional cable tension caused by vibrations.

2.2. Description of the Great Belt Bridge

One key structural characteristic of the East Great Belt Bridge (1998, DK) is the continuous girder deck over the full span of 2694 m [32]. Suspension bridges of this type are usually hinged at the pylons in order to accommodate an expansion joint there. The Great Belt similarly to the Humber, Severn and Bosporus Bridge has a streamlined box girder deck section, which is expected to display to an aerofoil heave-pitch flutter mode. The bridge has a cable sag ratio 1:9, chosen to reduce sliding forces in the anchorages. It is also interesting to note that for the two approach bridges, 32 tuned mass dampers were installed for suppressing vortex shedding, each having a mass of 8 t (approximately 0.5% of the modal mass). The structural parameters implemented in the FE model are presented in Table I.

2.3. Modal analysis results for the Great Belt Bridge

Figures 3 and 4 compare the natural frequencies and shapes of the vertical, lateral and torsional modes obtained by implementing the FE model developed with the modes shapes and natural frequencies reported in Larsen [32]. Further modal analyses of the Great Belt are given in [33], which are the product of more detailed FE modelling using commercial packages. The proposed mathematical formulation, however, results in a model of considerably lower size while staying within the uncertainty scatter of more complex models. An equal displacement on the main cables is expected because the model assumes inextensibility of the hangers. It might be worth noting that the antisymmetric deflections of the cable and the stiffening structures cause no additional cable tension H_w because the downward movement on onec side of the centreline of the centre span tends to increase the cable length, while at the same time,

DOI: 10.1002/stc

Table I. Structural properties of the finite element model of the Great Belt Bridge.

Element	Property	Value
Girder	Young modulus of elasticity	$E = 210 \times 10^9 N/m^2$
	Shear modulus of elasticity	$G = 80.8 \times 10^9 N/m^2$
	Element length	$L = 40$ m
	Half-chord width of the deck	$b = 15.5$ m
	girder mass	$m_g = 15\ 260$ kg/m
	Moment of inertia about horizontal axis	$I_y = 4$ m^4
	Moment of inertia about vertical axis	$I_z = 100$ m^4
	Torsional moment of inertia	$I_a = 7.6$ m^4
	Mass moment of inertia (including cables)	$I_m = 2.47 \times 10^6$ kgm^2/m
Cables	Young modulus of elasticity	$E_c = 210 \times 10^9$ N/m^2
	Cross-sectional area	$A_c = 0.44$ m^2
	Half-chord distance between cables	$b_c = 13.5$
	Diameter	$d_c = 0.75$ m
	Mass of the main cables (both cables)	$m_c = 2 \times 3745$ kg/m
	Horizontal cable tension (both cables)	$H_w = 2 \times 1.92 \times 10^8 N$
	Main cable sag	$f = 180$ m
	Length of shortest hanger cable	$h_{e,\min} = 10$ m

the upward movement on the other side of the centre span tends to reduce the cable length, and the effects balance each other. In consequence of the lack of additional cable tension, there is no interaction between the main and side spans for the antisymmetric modes due to the cables, and any movement of the side spans is due to the continuous girder assumption. In general, the structural model captures the necessary vertical and torsional modal characteristics of the structure, which are fundamental for the flutter instability analysis.

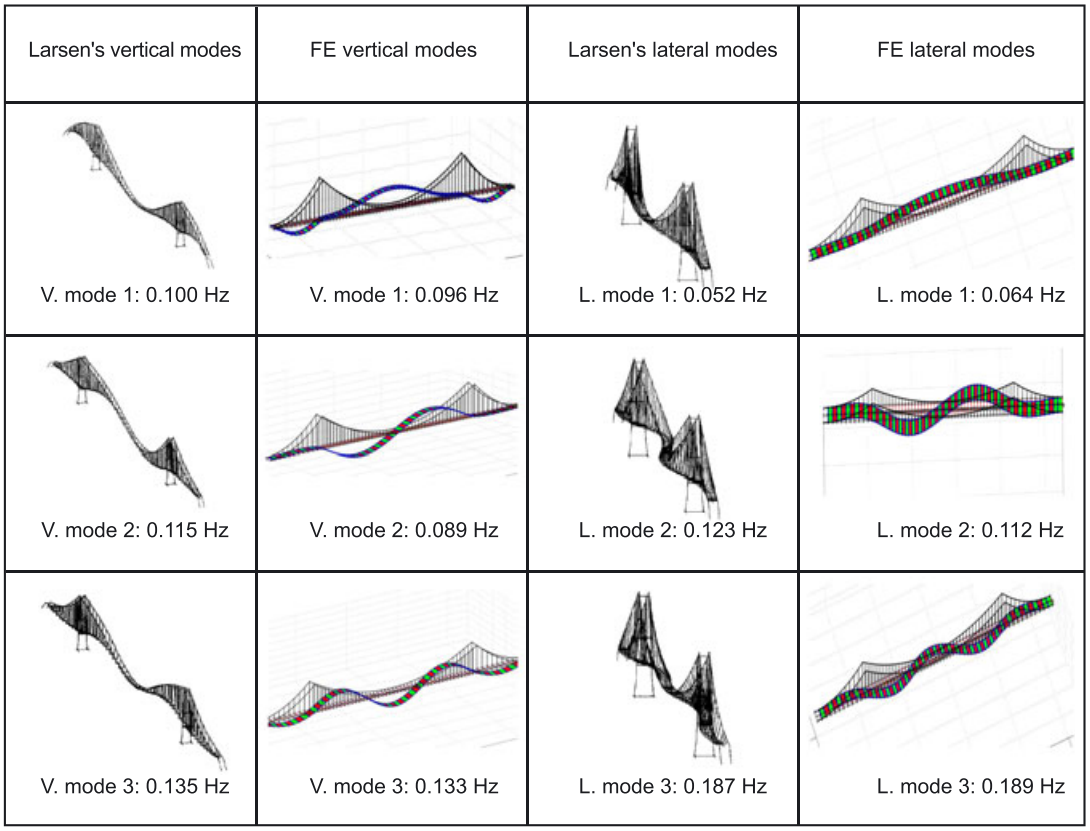

Figure 3. Comparison of experimentally identified vertical and lateral modes with FE results.

DOI: 10.1002/stc

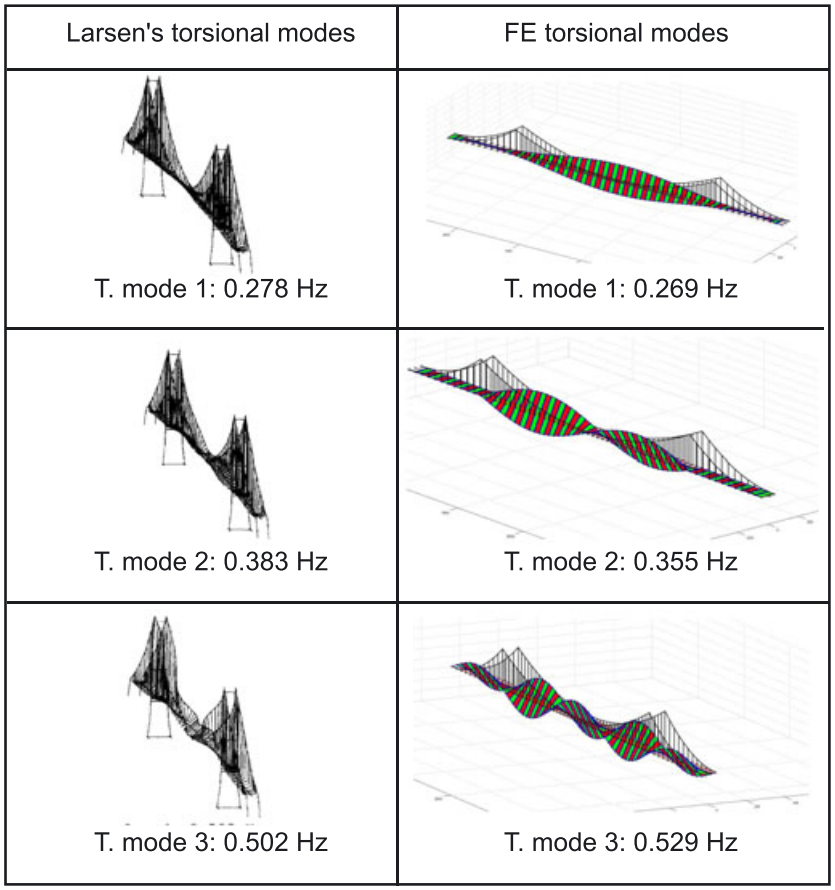

Figure 4. Comparison of experimentally identified torsional modes with FE results.

3. AEROELASTIC MODELS

In this section, we develop the FE aeroelastic model using the classical thin aerofoil theory as well as the flutter derivatives approach.

3.1. Sectional model with thin aerofoil theory

The lift L_{se} and moment M_{se} expressions presented for a thin aerofoil are taken from Theodorsen's original paper [27]:

$$L_{se} = -\pi\rho b^2\left[U\dot{\alpha} + \ddot{h}\right] - 2\pi\rho UbC(k)\left[U\alpha + \dot{h} + \frac{\dot{\alpha}b}{2}\right] \tag{3}$$

$$M_{se} = -\pi\rho b^2\left[\frac{bU\dot{\alpha}}{2} + \frac{b^2\ddot{\alpha}}{8}\right] + \pi\rho Ub^2C(k)\left[U\alpha + \dot{h} + \frac{b\dot{\alpha}}{2}\right] \tag{4}$$

where ρ is the mass of air per unit volume, b is the half chord of the wing, U is the wind velocity and $C(k)$ represents the Theodorsen circulation function:

$$C(k) = \frac{J_1(k) - iY_1(k)}{(J_1(k) + Y_0(k)) - i(Y_1(k) - J_0(k))} \tag{5}$$

in which $J_0(k), J_1(k), Y_0(k), Y_1(k)$ are Bessel functions of the first and second kind, respectively, $k = \omega b/U$ is the reduced frequency and $i = \sqrt{-1}$. The equations of motion of the sectional model (2-DOF aerofoil with heave and pitch) combined with the aerodynamic forces given in Equations (3) and (4) can be expressed in the following state–space form:

DOI: 10.1002/stc

$$\begin{bmatrix} 0 & M - M_{nc} \\ I & 0 \end{bmatrix} \begin{bmatrix} \dot{q} \\ \dot{q}_v \end{bmatrix} = \begin{bmatrix} -K & -C + C_{nc} \\ 0 & I \end{bmatrix} \begin{bmatrix} q \\ q_v \end{bmatrix} + \Xi_C \tag{6}$$

where Ξ_C represents the circulatory terms and

$$M = \begin{bmatrix} m & 0 \\ 0 & I_m \end{bmatrix} \qquad C = \begin{bmatrix} 2\omega_h m \zeta_h & 0 \\ 0 & 2\omega_a I_m \zeta_a \end{bmatrix} \qquad K = \begin{bmatrix} \omega_h^2 m & 0 \\ 0 & \omega_a^2 I_m \end{bmatrix} \tag{7}$$

$$M_{nc} = \begin{bmatrix} -\pi\rho b^2 & 0 \\ 0 & -\dfrac{\pi\rho b^4}{8} \end{bmatrix} \qquad C_{nc} = \begin{bmatrix} 0 & -\pi\rho b^2 U \\ 0 & -\dfrac{\pi\rho b^3 U}{2} \end{bmatrix} \tag{8}$$

with ω_h, ω_a the natural frequencies for the vertical/heave and torsional/pitch modes of the structure, ζ_h, ζ_a the corresponding critical damping ratios, q the position vector defined as $q = \{h, \alpha\}^T$ and q_v the velocity vector defined as $q_v = \left\{\dot{h}, \dot{\alpha}\right\}^T$. When introducing the state vector $x = \{q, q_v\}^T$, Equation (6) can be expressed in the form:

$$E_c \dot{x} = A_c x + \Xi_C \tag{9}$$

where

$$E_c = \begin{bmatrix} 0 & M - M_{nc} \\ I & 0 \end{bmatrix} \qquad A_c = \begin{bmatrix} -K & -C + C_{nc} \\ 0 & I \end{bmatrix} \tag{10}$$

Matrices M_{nc}, C_{nc} represent the non-circulatory part of the aerodynamic forces and are usually referred to as aerodynamic (or added) mass and damping matrices.

The circulatory term Ξ_C depends on the irrational function $C(k)$ and therefore cannot be expressed in a state space form. As a consequence, the traditional approach to aeroelastic stability analysis is based on finding iteratively windspeed(s) for which sinusoidal solutions to Equation (9) (or alternatively Equation (6)) exist. Standard algorithms, including the k-method and the p-k method [30], require the repeated evaluation of the circulation function $C(k)$ in Equation (5), which is a combination of Bessel functions. This approach has several disadvantages. First, one must seek out the resonant frequencies one at a time (one of which might be zero). Second, one must distinguish between single and coupled-mode cases – this becomes particularly inconvenient when high-order modal combinations are possible. Third, during a design exercise, one cannot form a clear picture as to how design changes are influencing the aeroelastic stability of the structure as a whole, which may possibly include multiple flutter modes as well as multiple divergence modes [21]. It is thus convenient to approximate the circulation function with a low-order rational function. Approximations of this type allow one to write the problem in a state space form and to replace the aforementioned methods with classic-theoretic analytic devices such as root-locus diagrams. By invoking a least squares approximation, an accurate quartic approximation of $C(k)$ was found:

$$C(k) = \frac{0.995 + 57.018(ik) + 23.788(ik)^2 + 1895.463(ik)^3 + 1523.247(ik)^4}{1 + 62.304(ik) + 807.784(ik)^2 + 3060.678(ik)^3 + 3033.763(ik)^4} \tag{11}$$

The Nyquist diagram of the Theodorsen circulation function, the often used Jones approximation [19] and the herein used quartic approximation are shown in Figure 5(a). Clearly, the quartic approximation is accurate, with the lower-order Jones function somewhat less so. Finally, employing the concepts of analytic continuation, ik in Equation (11) can be replaced with $\hat{s} = sb/U$, that is, the expression derived for oscillatory motion can be extended to use with arbitrary motion.

The circulatory term Ξ_C of the aerodynamic forces can be expressed mathematically by the feedback-loop system in Figure 5(b), in which the approximation of the circulation function $C(s)$ can be viewed as a transfer function that receives the structural response $y = U\alpha + \dot{h} + \dot{\alpha}b/U$ as input and generates the output $\tilde{y}$, which is finally translated into lift and moment by the factors $-2\pi\rho Ub$ and $\pi\rho Ub^2$. An equivalent state space realization $\tilde{A}, \tilde{B}, \tilde{C}, \tilde{D}$ of $C(s)$ is derived using standard techniques. Note that the number of (aerodynamic) states of such state space is four, because $C(s)$ is fourth order.

DOI: 10.1002/stc

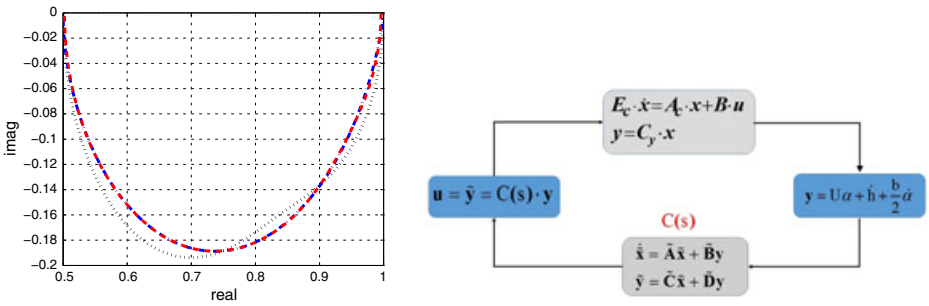

(a) (b)

Figure 5. (a) The Theodorsen function $C(k)$ and its rational approximations: the exact function is the (blue) dot-dash curve, the quartic approximation the (red) dashed curve and the Jones approximation the (black) dotted curve. (b) Block diagram of the open loop aerodynamic system of a 2 DOF sectional model.

The open-loop system dynamics for the sectional model including the circulatory terms are derived by augmenting the state space in Equation (9) to include the aerodynamic states related to the circulatory function:

$$E\dot{\hat{x}} = A\hat{x} \tag{12}$$

where

$$E = \begin{bmatrix} E_c & 0 \\ 0 & I \end{bmatrix} \quad A = \begin{bmatrix} A_c + B\tilde{D}C_y & B\tilde{C} \\ \tilde{B}C_y & \tilde{A} \end{bmatrix} \quad B = \begin{bmatrix} -2\pi\rho Ub \\ \pi\rho Ub^2 \\ 0 \\ 0 \end{bmatrix} \quad C_y = [0 \quad U \quad 1 \quad b/2] \tag{13}$$

with the matrices B and C_y explicitly derived from Equations (3) and (4) and $\hat{x}$consisting of the four 'structural' states (heave, pitch and related velocities) plus the four 'aerodynamic'. The eigenvalues of Equation (12) as a function of the wind speed U will determine the stability of the open-loop system. More specifically, the wind speed at which an eigenvalue has positive real part signifies the onset of an instability.

3.2. Finite element model with thin aerofoil theory

In order to include the aeroelastic forcing in a general FE formulation procedure, distributed lifting loading and distributed moments are considered for every element. The procedure followed here assumes lumping of the distributed forces on the nodes. The aerodynamic mass and damping matrices are now of dimension 12×12, with the non-zero entries corresponding to the heave and pitch-related degrees of freedom and can be superimposed at the corresponding degrees of freedom in the same way as the structural matrices:

$$M_a = \sum_{i=1}^{N} M_{nc,i} \qquad C_a = \sum_{i=1}^{N} C_{nc,i} \tag{14}$$

The equations of motion in a FE format now take the following form, similar to the case with 2-DOF sectional model in Equation (6):

$$\begin{bmatrix} 0 & M - M_a \\ I & 0 \end{bmatrix} \begin{bmatrix} \dot{Q} \\ \dot{Q}_v \end{bmatrix} = \begin{bmatrix} -K & -C + C_a \\ 0 & I \end{bmatrix} \begin{bmatrix} Q \\ Q_v \end{bmatrix} + \Xi_C \tag{15}$$

where Q is a vector containing the degrees of freedom of the bridge structure, Q_v the related velocities and the state vector is defined as $\hat{x} = \{Q, Q_v\}^T$. We then construct a feedback system with as many feedback loops as the number of elements used, (Figure 10).

In a similar manner as in the sectional model of Equation (12), the FE system dynamics are expressed in the form:

DOI: 10.1002/stc

$$E_g \dot{\hat{x}} = A_g \hat{x} \tag{16}$$

where

$$E_g = \begin{bmatrix} E_c & 0 \\ 0 & I \end{bmatrix} \qquad A_g = \begin{bmatrix} A_c + B_g \widetilde{D}_g C_g & B_g \widetilde{C}_g \\ \widetilde{B}_g C_g & \widetilde{A}_g \end{bmatrix} \tag{17}$$

in which $\tilde{A}_g = \mathrm{diag}(\tilde{A}), \tilde{B}_g = \mathrm{diag}(\tilde{B}), \tilde{C}_g = \mathrm{diag}(\tilde{C}), \tilde{D}_g = \mathrm{diag}(\tilde{D})$ and $\hat{x}$ consists of the structural states, their velocities and the aerodynamic states related to the circulatory functions (namely, there are four aerodynamic states for each of the FE of the model, because there is a circulatory function for each element).

3.3. Great Belt Bridge with thin aerofoil theory

The Great Belt Bridge was again used in order to implement the aeroelastic FE procedure. The structural damping matrix is assessed by assuming a Rayleigh proportional damping model $C = a_M M + a_K K$. The parameters a_M, a_K are chosen so as to result in a 1 % critical damping ratio for the first vertical and torsional mode. Figure 6 presents the open-loop root locus diagram of the Great Belt Bridge, in which the wind velocity U is the varied parameter. From the diagram, one can observe two instability modes, which cross into the real positive plane of the calculated eigenvalues. One presents itself as a complex pair of eigenvalues and corresponds to an oscillatory divergent motion (flutter), whereas the other has real eigenvalues and consequently presents a monotonically increasing instability due to steady-state aerodynamic moment. As shown in Figure 6, the Great Belt Bridge model reaches flutter instability at 82 m/s and torsional divergence at 90 m/s.

Flutter speed estimates for the Great Belt Bridge have been reported elsewhere [33], but these predictions have a large scatter, ranging from 62 to 97 m/s. Table II gives a summary of these results as well as the values predicted by the proposed analytical framework. Flutter speeds based on an equivalent 2-DOF, heave-pitch model, both using thin aerofoil theory and flutter derivatives, are included. The predicted flutter speed using the 2-DOF model is the same as Larsen analytic flutter prediction using flutter derivatives (measured on a sectional model) [32], which was based on a two-mode routine with allowance for the mode shapes of the basic symmetric bending and torsion mode. The higher critical wind speeds obtained with the full structural modes can be attributed to multimodal behaviour, with higher vertical modes participating in the first flutter mode as will be discussed in Section 5.

3.4. Finite element model with flutter derivatives

Theodorsen's approach of using velocity potentials due to the air flow around the deck and adoption of the Kutta condition [35] may result in significant errors if the deck girder is considered to fall into the bluff body category; for this reason, the use of the so-called flutter derivatives was introduced by Scanlan [36]. There are several different formulations using different combinations of k, K, b, B. In this

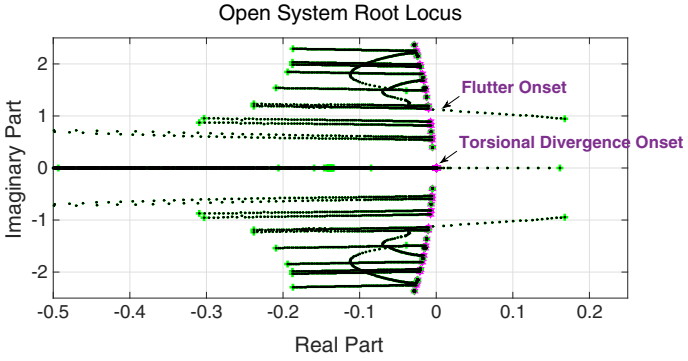

Figure 6. Root-locus of the Great Belt Bridge. The wind speed is swept from 0 (magenta hexagon) to 100 m/s (green cross). The flutter mode goes unstable at 82 m/s, while the torsional divergence mode goes unstable at 90 m/s.

DOI: 10.1002/stc

Table II. Estimation of flutter velocities of the Great Belt Bridge from literature.

Reference	Flutter velocity
Jurado *et al.* [33]: numerical, flutter derivatives, two modes	90 m/s
Jurado *et al.* [33]: numerical, flutter derivatives, 18 modes	62 m/s
Cobo [34]: numerical, flutter derivatives, two modes	83 m/s
Cobo [34]: numerical, flutter derivatives, six modes	97 m/s
Larsen [32]: wind tunnel section model	70–74 m/s
Larsen [32]: wind tunnel taut strip model	72 m/s
Larsen [32]: wind tunnel full bridge model	70–75 m/s
Larsen [32]: numerical, flutter derivatives from section model	75 m/s
Larsen [32]: numerical, flutter derivatives from taut strip model	79 m/s
This work: numerical, flutter derivatives, all modes	81 m/s
This work: numerical, thin aerofoil, all modes	82 m/s
This work: numerical, flutter derivatives, two modes	75 m/s
This work: numerical, thin aerofoil, two modes	75 m/s

work, we adopt the following notation:

$$L_{se} = \frac{1}{2}\rho U^2 B\left[KH_1^*\left(\frac{\dot{h}}{U}\right) + KH_2^* B\left(\frac{\dot{\alpha}}{U}\right) + K^2 H_3^*\alpha + K^2 H_4^*\left(\frac{h}{B}\right)\right] \tag{18}$$

$$M_{se} = \frac{1}{2}\rho U^2 B^2\left[KA_1^*\left(\frac{\dot{h}}{U}\right) + KA_2^* B\left(\frac{\dot{\alpha}}{U}\right) + K^2 A_3^*\alpha + K^2 A_4^*\left(\frac{h}{B}\right)\right] \tag{19}$$

where H_1^*, A_1^* are the dimensionless flutter derivatives, which are a function of the reduced frequency $K = \omega B/U$, ω is the circular frequency and $B = 2b$ is the deck width. In this formulation, the drag degree of freedom is omitted because our aim is to compare this procedure with the thin aerofoil theory. However, the drag effect has been shown to be important for certain cases like for the truss-decked Akashi-Kaikyo Bridge, the world's longest suspension bridge [37]. The theoretical values of the flutter derivatives of a thin aerofoil can be computed in terms of the Theodorsen circulation function giving the following expressions [38]:

$$\begin{aligned}
H_1^* &= -2\pi F(k)/K & A_1^* &= \pi F(k)/2K \\
H_2^* &= -\frac{\pi}{2K}\left[1 + \frac{4G(k)}{K} + F(k)\right] & A_2^* &= -\frac{\pi}{2K^2}\left[\frac{K}{4} - G(k) - \frac{KF(k)}{4}\right] \\
H_3^* &= -\frac{\pi}{K^2}\left[2F(k) - \frac{1}{2}GK\right] & A_3^* &= \frac{\pi}{2K^2}\left[\frac{K^2}{32} + F(k) - \frac{KG(k)}{4}\right] \\
H_4^* &= \frac{\pi}{2}\left[1 + \frac{4G}{K}\right] & A_4^* &= -\pi G(k)/2K
\end{aligned} \tag{20}$$

where $K = 2k = 2\omega b/U$ and $F(k), G(k)$ are the real and imaginary parts of the Theodorsen function $C(k) = F(k) + iG(k)$. Equations (18) and (19) can be rewritten in a matrix form:

$$\begin{aligned}
\begin{Bmatrix} L_{se} \\ M_{se} \end{Bmatrix} = \frac{1}{2}\rho U^2 B\begin{bmatrix} \frac{KH_1^*}{U} & KH_2^*\frac{B}{U} \\ \frac{BKA_1^*}{U} & BKA_2^*\frac{B}{U} \end{bmatrix}\begin{Bmatrix} \dot{h} \\ \dot{\alpha} \end{Bmatrix} \\
+\frac{1}{2}\rho U^2 B\begin{bmatrix} \frac{K^2 H_4^*}{B} & K^2 H_3^* \\ K^2 A_4^* & K^2 A_3^* B \end{bmatrix}\begin{Bmatrix} h \\ \alpha \end{Bmatrix}
\end{aligned} \tag{21}$$

Equation (21) can now be expressed in the frequency domain ($\dot{h} = i\omega h, \dot{\alpha} = i\omega\alpha$), and the RFA $Q(iK)$ of the resulting matrix can be introduced:

DOI: 10.1002/stc

$$\begin{Bmatrix} L_{se} \\ M_{se} \end{Bmatrix} = \frac{1}{2}\rho U^2 \begin{bmatrix} K^2H_4^* + iK^2H_1^* & B\left[K^2H_3^* + iK^2H_2^*\right] \\ B\left[K^2A_4^* + iK^2A_1^*\right] & B^2\left[K^2A_3^* + iK^2A_2^*\right] \end{bmatrix} \begin{Bmatrix} h \\ \alpha \end{Bmatrix} = U^2 \cdot Q(iK) \cdot \begin{Bmatrix} h \\ \alpha \end{Bmatrix} \tag{22}$$

in this work, the so-called Roger's approximation [29] is employed:

$$\hat{Q}(iK) = P_0 + P_1 \cdot iK + P_2 \cdot (iK)^2 + \sum_{j=3}^{N} \frac{P_j \cdot iK}{iK + \gamma_{j-2}} \tag{23}$$

where the matrices P_0, P_1, P_2, P_j and the coefficients γ_{j-2} are frequency-independent and are found by fitting against the wind tunnel experimental data of the deck section model. Note that P_0, P_1, P_2 are the non-circulatory stiffness, damping and inertia (added-mass), while P_j, γ_{j-2} are related to the circulatory forces.

In the present work, we use four poles, that is, $N-2=4$. Similarly to the case of thin aerofoil theory, iK in Equation (23) can be replaced with $\hat{s} = sB/U$. The equations of motion for the sectional model can now be rewritten in the Laplace domain as

$$\begin{aligned} (Ms^2 + Cs + K)q(s) &= U^2 \hat{Q}(\hat{s}) q(s) \\ &= U^2 \left(P_0 + P_1 s\frac{B}{U} + P_2 s^2 \left(\frac{B}{U}\right)^2 + \sum_{j=3}^{N} \frac{P_j \cdot s\frac{B}{U}}{s\frac{B}{U} + \gamma_{j-2}} \right) q(s) \end{aligned} \tag{24}$$

Equation (24) is converted back to the state space form by taking the inverse Laplace transform. In particular, note that the inverse Laplace transform of the circulatory terms (normalized by U^2P_j) reads:

$$X_{aj}(s) = \frac{s\frac{B}{U}}{s\frac{B}{U} + \gamma_{j-2}} q(s) \overset{\mathscr{L}^{-1}}{\rightarrow} \dot{X}_{aj}(t) = \dot{q}(t) - \frac{U}{B}\gamma_{j-2} X_{aj}(t) \tag{25}$$

where $X_{aj}(t)$ is the aerodynamic state associated with the circulatory term, which adds the structural states q. Therefore, the system equations in the time domain are

$$\begin{Bmatrix} \dot{q} \\ \ddot{q} \\ \dot{X}_{a3} \\ \dot{X}_{a4} \\ \dot{X}_{a5} \\ \dot{X}_{a6} \end{Bmatrix} = \begin{bmatrix} 0 & I & 0 & 0 & 0 & 0 \\ -\overline{M}^{-1}\overline{K} & -\overline{M}^{-1}\overline{C} & U^2\overline{M}^{-1}P_3 & U^2\overline{M}^{-1}P_4 & U^2\overline{M}^{-1}P_5 & U^2\overline{M}^{-1}P_6 \\ 0 & I & -\left(\frac{U}{B}\right)\gamma_1 I & 0 & 0 & 0 \\ 0 & I & 0 & -\left(\frac{U}{B}\right)\gamma_2 I & 0 & 0 \\ 0 & I & 0 & 0 & -\left(\frac{U}{B}\right)\gamma_3 I & 0 \\ 0 & I & 0 & 0 & 0 & -\left(\frac{U}{B}\right)\gamma_4 I \end{bmatrix} \begin{Bmatrix} q \\ \dot{q} \\ X_{a3} \\ X_{a4} \\ X_{a5} \\ X_{a6} \end{Bmatrix} \tag{26}$$

where $\overline{M} = M - U^2P_2\left(\frac{B}{U}\right)^2$, $\overline{C} = C - U^2P_1\left(\frac{B}{U}\right)$, $\overline{K} = K - U^2P_0$.

Similar to the case of the thin aerofoil theory, the flutter derivatives approach can be extended to an FE form, where again, the lift and moment equations, Equations (18) and (19), are lumped at the end nodes of every element. For the FE model, the elemental matrices P_{0e}, P_{1e}, P_{2e} related to the non-circulatory components have dimensions 12 × 12 and can be superimposed similarly to the structural matrices:

DOI: 10.1002/stc

$$P_{0G} = \sum_{i=1}^{N} P_{0e,i} \qquad P_{1G} = \sum_{i=1}^{N} P_{1e,i} \qquad P_{2G} = \sum_{i=1}^{N} P_{2e,i} \tag{27}$$

where the summation is again intended in the FE sense. Because the aerodynamic states $X_{aj}, j = 3..6$ are related to the pitch and heave of every node, the matrices $P_{je}, j = 3..6$ have size 12×4:

$$P_j = \begin{pmatrix} P_j^{11} & P_j^{12} \\ P_j^{21} & P_j^{22} \end{pmatrix} \quad \rightarrow \quad P_{je} = \frac{L}{2} \begin{pmatrix} \underbrace{P_j^{11}}_{heave} & P_j^{12} & 0 & 0 \\ \vdots & \vdots & \vdots & \vdots \\ P_j^{21} & \underbrace{P_j^{22}}_{pitch} & 0 & 0 \\ 0 & 0 & \underbrace{P_j^{11}}_{heave} & P_j^{12} \\ \vdots & \vdots & \vdots & \vdots \\ 0 & 0 & P_j^{21} & \underbrace{P_j^{22}}_{pitch} \end{pmatrix} \tag{28}$$

It is worth noting at this stage that this formulation introduces eight extra aerodynamic states per node (four related to the pitch and four related to the heave, because the flutter derivatives were approximated using four poles) as opposed to the case of thin aerofoil, which introduces just four (related to the four poles used to approximate the Theodorsen function).

3.5. Application and comparison of flutter derivatives to the Great Belt Bridge

We implement the procedure described in Section 3.3 for the experimental data obtained at the water channel of the University of Hamburg, reported in Starossek *et al.* [39] and later in [35]. Figure 7 presents the approximation for the four terms of the matrix $\underline{Q}$ in Equation (23) when thin aerofoil theory and experimental derivatives from the Great Belt are used. The RFA as shown in Figure 7(a) results in a very good fit when thin aerofoil theory is used because the points fall on smooth lines. For the experimental data, irregularities pose difficulties in fitting, but still, the results are reasonably good (Figure 7(b)). These can of course be improved with an increasing number of aerodynamic poles, which in turn though increases the dimensions of the state space. A nonlinear least square procedure was also implemented in the approximation where the location of the poles was not preselected but optimized; however, this yielded only a marginally better improvement of the fitting.

Figure 8 presents a comparison of the root-loci of the full bridge when using thin aerofoil theory, namely Figure 6, and flutter derivatives. The similarity of aerodynamic behaviour and the assumption that the streamlined box girder under investigation resembles the behaviour of a thin aerofoil are apparent. Both thin aerofoil theory and the use of flutter derivatives are very close in their prediction of the flutter critical wind speed (81 m/s vs 82 m/s).

The lift and moment on the system including leading-edge and trailing-edge flaps were based on a transformation of the wing–aileron–tab configuration [40]. The transformation is depicted in Figure 9. In this new configuration, the aileron becomes the bridge deck, the wing is the leading-edge flap and the tab is the trailing-edge flap. In order to re-level the bridge and return its mass centre to the correct position, pitch-and-heave correction must be applied. For the system depicted in Figure 9, the inertial properties of the flaps were neglected and only their aerodynamic influence on the lift and moment applied on the deck was considered. This is a mathematically simplifying assumption based on the premise that the mass of the flaps should be kept considerably smaller that the mass of the deck in order to minimize the additional dead load. In a similar manner as for the case of sole deck, Equation (12) holds, with the aerodynamic mass, damping and stiffness matrices are formed as follows:

DOI: 10.1002/stc

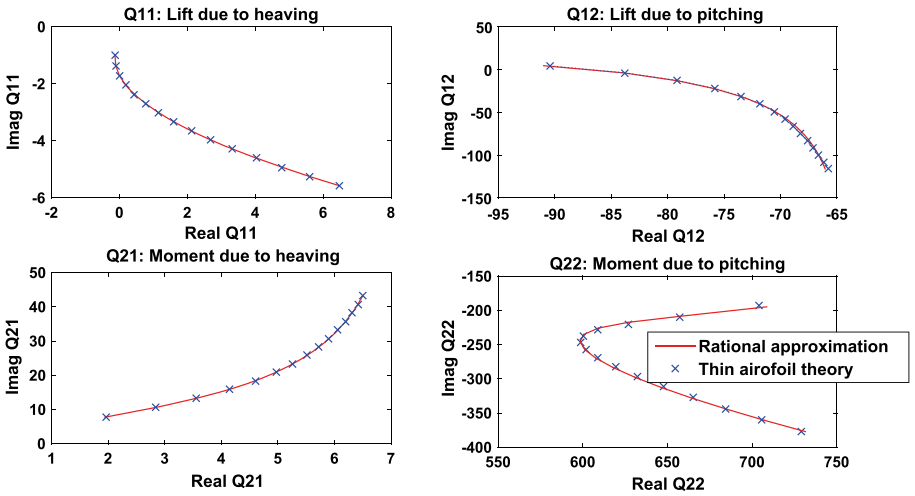

(a)

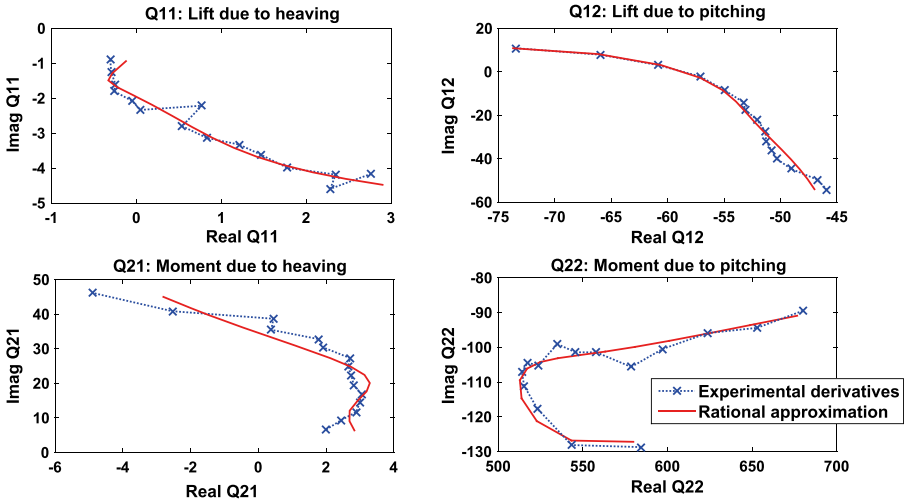

(b)

Figure 7. Roger's approximation for the four terms of $\hat{Q}$when (a) thin aerofoil and (b) experimental flutter derivatives are implemented.

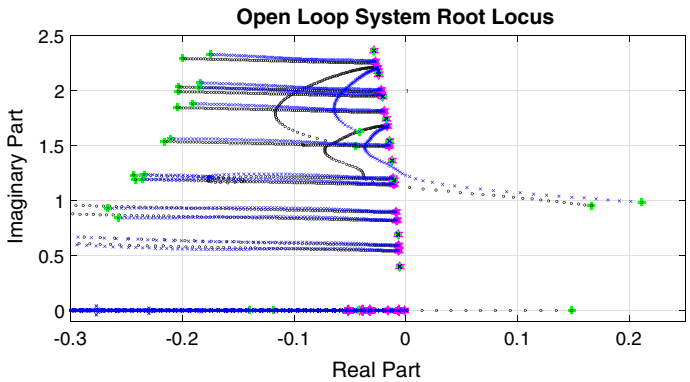

Figure 8. Comparison of root-loci for the Great Belt Bridge using thin aerofoil theory and flutter derivatives. The wind is swept from 0 (magenta hexagon) to 100 m/s (green cross). The black circles correspond to the use of thin aerofoil theory, and the blue crosses to the use of flutter derivatives. Thin aerofoil theory predicts flutter at 82 m/s and flutter derivatives at 81 m/s.

DOI: 10.1002/stc

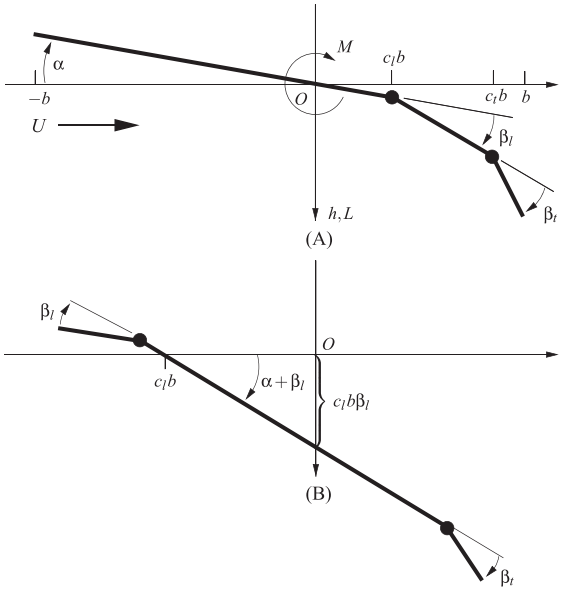

Figure 9. Transformation of the Theodorsen–Garrick wing–aileron–tab configuration into a controlled bridge deck. (a) The wing pitch angle is α, the aileron angle is β_l and the tap angle is β_t, U denotes the wind speed. (b) The leading flap angle is β_l, the deck angle is α and the trailing-edge flap angle is β_t.

$$M_{ncF} = \begin{bmatrix} -\pi\rho b^2 & 0 & M_{ncF}^{1,3} & M_{ncF}^{1,4} \\ 0 & -\dfrac{\pi\rho b^4}{8} & M_{ncF}^{2,3} & M_{ncF}^{2,4} \\ 0 & 0 & 0 & 0 \\ 0 & 0 & 0 & 0 \end{bmatrix} \tag{29}$$

$$C_{ncF} = \begin{bmatrix} 0 & -\pi\rho b^2 U & C_{ncF}^{1,3} & C_{ncF}^{1,4} \\ 0 & -\dfrac{\pi}{2}\rho b^3 U & C_{ncF}^{2,3} & C_{ncF}^{2,4} \\ 0 & 0 & 0 & 0 \\ 0 & 0 & 0 & 0 \end{bmatrix} \tag{30}$$

$$K_{ncF} = \begin{bmatrix} 0 & 0 & K_{ncF}^{1,3} & K_{ncF}^{1,4} \\ 0 & 0 & K_{ncF}^{2,3} & K_{ncF}^{2,4} \\ 0 & 0 & 0 & 0 \\ 0 & 0 & 0 & 0 \end{bmatrix} \tag{31}$$

where

$$M_{ncF}^{1,3} = \rho b^3 T_1(c_t) \tag{32}$$

$$M_{ncF}^{1,4} = \rho b^3 (T_1(c_l) - \pi c_l) \tag{33}$$

$$M_{ncF}^{2,3} = \rho b^4 (T_7(c_t) + c_t T_1(c_t)) \tag{34}$$

$$M_{ncF}^{2,4} = \rho b^4 \left(T - T_7(c_l) + c_l T_1(c_l) + \frac{\pi}{8} \right) \tag{35}$$

$$C_{ncF}^{1,3} = \rho U b^2 T_4(c_t) \tag{36}$$

DOI: 10.1002/stc

$$C_{ncF}^{1,4} = \rho U b^2 (T_4(c_t) + \pi) \tag{37}$$

$$C_{ncF}^{2,3} = -\rho b^3 U \left[T_1(c_t) - T_8(c_t) - c_t T_4(c_t) + T_{11}\left(\frac{c_t}{2}\right) \right] \tag{38}$$

$$C_{ncF}^{2,4} = -\rho b^3 U \left[T_1(c_l) - T_8(c_l) - c_l T_4(c_l) + T_{11}\left(\frac{c_l}{2}\right) - \frac{\pi}{2} \right] \tag{39}$$

$$K_{ncF}^{1,3} = K_{ncF}^{1,4} = 0 \tag{40}$$

$$K_{ncF}^{2,3} = -\rho b^2 U^2 (T_4(c_t) + T_{10}(c_t)) \tag{41}$$

$$K_{ncF}^{2,4} = -\rho b^2 U^2 (T_4(c_l) + T_{10}(c_l)) \tag{42}$$

The terms T_{ij} are given in [40]. The size of M_{ncF}, C_{ncF} is 4×4. Indeed, there are two additional columns related to the flap angles β_t, β_l (note that the upper left 2×2 submatrices are exactly those reported in Equation (8)) and two additional zero rows corresponding to the equations of motion related to the flap angles. Note that the structural M, C, K matrices are now enlarged to be 4×4 (and named M_F, C_F, K_F), to include the equations related to the flaps. Moreover, in this case, these additional rows/columns are zero, because the flaps have been assumed massless and neither damping nor stiffness is considered.

The matrices B_F, C_{yF} (corresponding to the old B and C_y in Equation (13)) are now given by

$$B_F^T = \begin{bmatrix} -2\pi\rho U b & \pi\rho U b^2 & 0 & 0 & 0 & 0 & 0 & 0 \end{bmatrix} \tag{43}$$

$$C_{yF} = \begin{bmatrix} 0 & U & T_{10}(c_t)\dfrac{U}{\pi} & T_{10}(c_l)\dfrac{U}{\pi} - U & 1 & \dfrac{b}{2} & T_{11}(c_t)\dfrac{b}{2\pi} & T_{11}(c_l)\dfrac{b}{2\pi} + b\left(c_l - \dfrac{1}{2}\right) \end{bmatrix} \tag{44}$$

The aeroelastic model of the bridge including the flaps is thus cast into a generalized state space form, again similar to the case of sole deck in Equation (12), and the corresponding 8×8 E_c, A_c matrices are

$$E_c = \begin{bmatrix} 0 & M_F - M_{\text{ncF}} \\ I & 0 \end{bmatrix} \qquad A_c = \begin{bmatrix} -K_F + K_{\text{ncF}} & -C_F + C_{\text{ncF}} \\ 0 & I \end{bmatrix} \tag{45}$$

The state vector is now $x = \left\{ h, \alpha, \beta_t, \beta_l, \dot{h}, \dot{\alpha}, \dot{\beta}_t, \dot{\beta}_l \right\}^T$.

When extending this procedure to the case of FE, Equation (16) still applies, but the state vector is now augmented to ${}^{x} = \{Q, F, Q_v, , F_v\}^T$, where F and F_v are all of the flap and angles and their derivatives, respectively. Note that in this case, some elements consist of just the deck (i.e. $M_{ncF} = C_{ncF} = K_{ncF} = 0$ and $C_{yF} = [0, U, 0, 0, 1, b/2, 0, 0]$), and some include the flaps.

4. CONTROL DESIGN

We now consider the general case of a bridge having n segments put in place and k of them having trailing-edge and leading-edge flaps (Figure 10). The uncontrolled (open-loop) system is described by the aeroelastic model $P(s)$ (corresponding to the state space matrices E_g, A_g, B_g, C_z), and the leading-edge and trailing-edge flaps controllers are denoted as $k_{li}(s)$ and $k_{ti}(s)$. Both controllers receive the pitch angle α_i of the corresponding element as their input and generate the flap angles β_{li}, β_{ti} as output. The generalized state–space model is given as

$$E_g \dot{\hat{x}} = A_g x + B_g u \tag{46}$$

$$z = C_z \hat{x} \tag{47}$$

where $u = \{\beta_{t1}, \beta_{l1}, \ldots, \beta_{tk}, \beta_{lk}\}^T$ and $z = \{\alpha_1, \ldots \alpha_k\}^T$. Because the controlled inputs are the flap angles rather than torques to massy flap bodies, the model given in Equations (46) and (47) must generate

DOI: 10.1002/stc

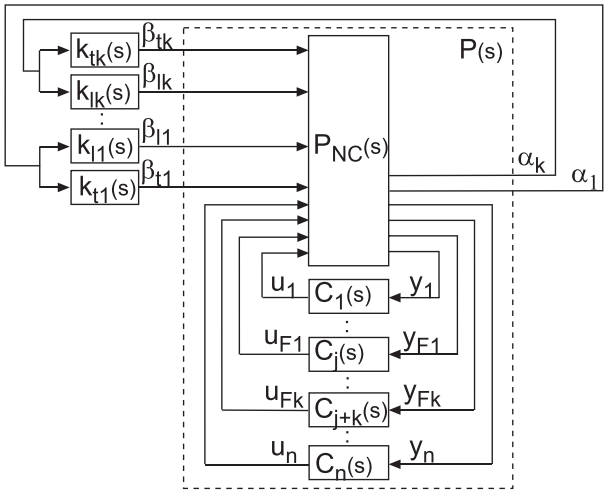

Figure 10. Block diagram of the system. $P_{NC}(s)$ is the aeroelastic model without the circulatory terms, $P(s)$ is the aeroelastic model (the $C_i(s)$ feedbacks are for the inclusion of the circulatory terms), $k_{li}(s)$ and $k_{ti}(s)$ are the compensators of the leading and trailing flaps, α_i are the pitch angles and β_{li} and β_{ti} are the leading-edge and trailing-edge flap angles.

the first and second derivatives of the flap angles internally; these derivatives are required by the aerodynamic model. This is achieved using a generalized state space system of the form:

$$\begin{bmatrix} 0 & 0 \\ 1 & 0 \end{bmatrix} \begin{bmatrix} \dot{x}_1 \\ \dot{x}_2 \end{bmatrix} = \begin{bmatrix} 1 & 0 \\ 0 & 1 \end{bmatrix} \begin{bmatrix} x_1 \\ x_2 \end{bmatrix} + \begin{bmatrix} -1 \\ 0 \end{bmatrix} \beta \tag{48}$$

in which β represents each flap angle. It follows immediately that

$$x_1 = \beta \qquad x_2 = \dot{\beta} \qquad \dot{x}_2 = \ddot{\beta} \tag{49}$$

Note that these equations are introduced in the state–space model at the rows corresponding to the flap angles β_{ti}, β_{li} (first row of Equation (48)) and their derivatives $\dot{\beta}_{ti}, \dot{\beta}_{li}$ (second row of Equation (48)). Because Equation (48) has both its eigenvalues at infinity, the system will have $4k$ eigenvalues there. These eigenvalues are not associated with 'real' system dynamics, or system stability properties, and are thus ignored throughout the paper.

We now design the controller characteristics for the leading-edge and trailing-edge flaps that result in a closed-loop stable system with maximum robustness margin. The higher the stability robustness margin is, the larger the uncertainties (e.g. variations in the model and/or in its parameters) that the controlled system can cope with while remaining stable. This is an essential requirement because, ultimately, it is the bridge and not the bridge model that must be stabilized. In recent years, there has been growing interest in control design of structural systems under the presence of structured or unstructured uncertainties. In [41], for example, the vibration control of a tensegrity structure was considered using H_∞ robust control theory and μ synthesis.

Different robustness criteria can be used, for example, robustness to additive and/or multiplicative perturbation on the plant P, on the controller K, on the loop transfer function PK and so on. In this work, we use robustness to coprime perturbation because this combines advantages from several different robustness criteria [42,43], it can for example account for uncertainty on lightly damped natural frequencies, which play a pivotal role in the system's dynamics. Optimizing for additive perturbation on the plant P is known to give controllers with poor gain margins but places a favourable explicit limit on the high-frequency gain of the resulting controller. On the other hand, an index related to multiplicative perturbation on P is known to give good robustness margin but may have unbounded high-frequency gain.

The normalized left coprime factorization of the plant P is defined as

$$P = M^{-1}N \tag{50}$$

where $M, N \in H_\infty$ and

$$MM^{\sim} + NN^{\sim} = I \tag{51}$$

DOI: 10.1002/stc

$(\cdot)^{\sim}$ means adjoint. The perturbed plant is

$$P_{\Delta} = (M - \Delta_M)^{-1}(N + \Delta_N) \tag{52}$$

The aim is to design a stabilizing controller that maximizes the size of admissible perturbation:

$$\left\| \Delta_M \quad \Delta_N \right\|_{\infty} < \gamma^{-1} \tag{53}$$

thereby minimizing the achievable value of γ [42,43]:

$$\left\| \begin{bmatrix} K \\ I \end{bmatrix} (I - PK)^{-1} [P \quad I] \right\|_{\infty} < \gamma = \frac{1}{\epsilon} \tag{54}$$

In practice, the objective is to find a stabilizing feedback controller that minimizes γ while satisfying Equation (54) (ϵ is called normalized coprime stability margin or gap metric stability margin). Note that it is always $\gamma \geq 1$. It is worth noting that minimizing γ results in a bounded ∞-norm for KS, S, KSP, SP (these terms are the four submatrices obtained when expanding the left-hand side of Equation (54)), where $S = (1 - PK)^{-1}$. These terms are robust stability indexes: the lower their norm, the better the related robustness. In particular, $\|KS\|_{\infty}$ is related to the robustness against additive perturbation on the plant P, $\|S\|_{\infty}$ is related to the robustness against additive perturbation on the loop transfer function PK, $\|KSP\|_{\infty}$ is related to the robustness against multiplicative perturbation on the controller K and $\|SP\|_{\infty}$ is related to the robustness against additive perturbation on controller K.

We use the H_{∞} control theory framework to solve this robust stabilization problem. This will result in the optimal controller, that is, the (active) controller that gives the maximum/best stability robustness and will serve as a reference for simpler controllers, for example, lower-order and/or passive controllers. A characteristic of the H_{∞} optimal controller is that it has a size equal to that of the plant reduced by at least one. Many times, controllers that are slightly suboptimal (i.e. controllers giving $\gamma > \gamma_{min}$) are derived for a number of reasons (numerically easier to derive, smaller gains, etc.). These controllers have the same degree of the plant. It is now clear that, in general, these optimal and suboptimal controllers are complex and have a very high degree. However, model reduction techniques on model and/or controller can be implemented for practical implementation [42,43].

5. DESIGN EXAMPLE

Because the critical flutter and divergence speed of the Great Belt Bridge are already very high, a longer version of the bridge was created. All the parameters in Table I are kept the same, but for this case, the main span has a length of $L_m = 2400$ m (instead of 1620 m), the cable sag is $f = 260$ m (instead of 180 m) and the length of the shortest hanger remains $h_{e,\min} = 10$ m. In practice, the main span and the towers have been upscaled by 50 %, while the same deck section is kept the same. The controllable winglets are concentrated in the middle of the main span so as to suppress the first critical flutter mode and are considered to be an integral part of the deck as shown in Figure 11.

For this bridge example, the flutter and divergence speed using thin aerofoil theory is estimated at 57 m/s and 68 m/s, respectively. As shown in the left-hand part in Figure 12, there is a second flutter mode becoming unstable at 73 m/s. Each point on the root-locus diagram corresponds to a mode of the system at a specific wind speed. The right-hand part in Figure 12 presents the natural frequency and the damping ratio of different modes along the first instability path. Negative aerodynamic damping

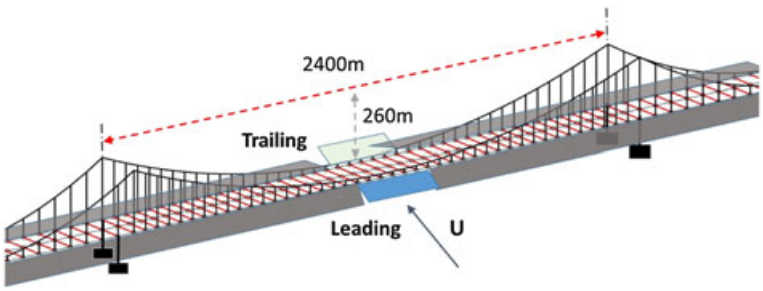

Figure 11. Bridge with flaps considered to be an integral part of the deck.

DOI: 10.1002/stc

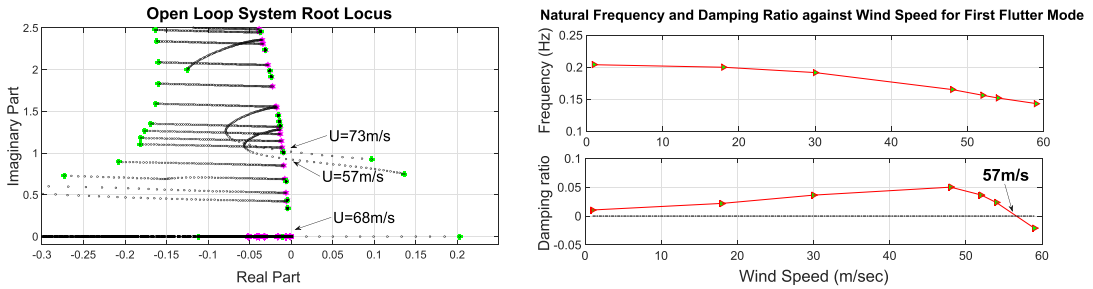

Figure 12. (a) Root locus of the 2400 m main span bridge example. The first flutter mode becomes unstable at 57 m/s and the second one at 73 m/s. The torsional divergence mode reaches instability at 68 m/s. (b) Natural frequency (Hz) and damping ratio for different wind speeds along the first flutter mode. The system becomes unstable when damping is negative.

signifies the onset of an aeroelastic instability, and the corresponding wind speed is indicated on the plot. At zero wind speed, the natural frequency and damping ratio is that of the first torsional mode, while the following points do not correspond to a pure structural mode because the airflow alters the system.

For points along instability paths, the corresponding complex eigenvectors are extracted to give insight in the mode coupling, which results in aerodynamic instability. Figure 13 presents the normalized vertical projection of the complex vertical and torsional real components of the mode for the two flutter instabilities. The left part in Figure 13 (first flutter mode) reveals the contribution of higher vertical modes near flutter speed.

The goal in this design exercise is to determine the minimum flap area that needed stretching from the midpoint of the main span to restore the stability limits to that of the Great Belt Bridge. The system's robust stability margins up to wind speed of 80 m/s are examined while varying the length of the flaps. As a first step, we follow a simplified procedure for the controller design as we optimize for coprime robustness on the equivalent sectional model (Figure 14). Figure 15(a) presents the robustness index γ

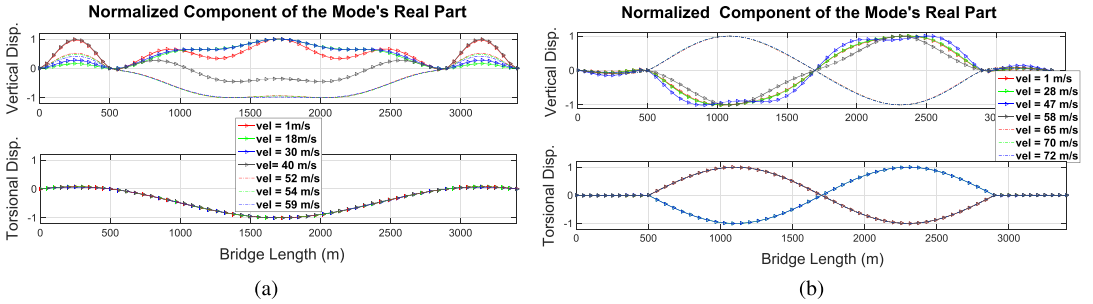

Figure 13. Mode shape of (a) the first flutter mode and (b) the second flutter mode.

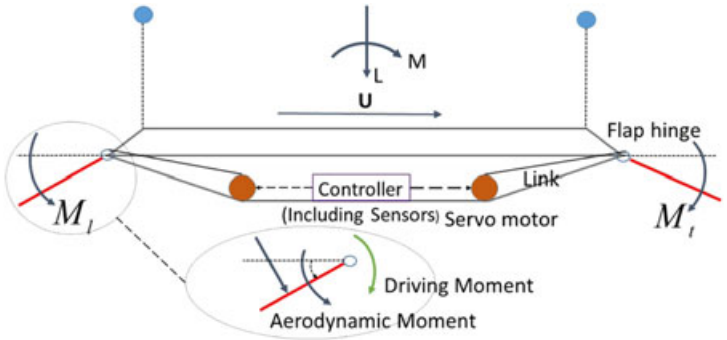

Figure 14. Sketch of the practical implementation of the active control system to the bridge deck. The pitch of the deck is monitored, and the control signals are transmitted to the servo motors that determine the rotation angles of the leading and trailing flaps.

DOI: 10.1002/stc

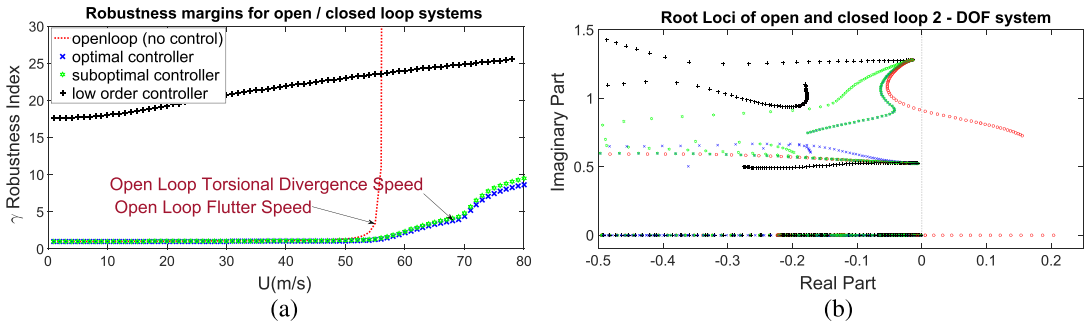

Figure 15. (a) Robustness index as a function of wind speed for different control configurations and (b) corresponding root loci diagrams for the different controllers.

of the sectional model as a function of wind speed for the case of the open-loop system (no control) as well as for different control configurations. In this case, the trailing-edge and leading-edge flaps have a width of 3 m each. The blue crosses correspond to the optimal H_∞ controller, optimized for coprime robustness at every wind speed (adaptive). These controllers are of the ninth order, which is slightly smaller than that of the plant which is 12th order. Green hexagons indicate the robustness index for suboptimal controllers, designed to have a γ that is 10 % larger than the optimal γ. Again, they are designed for every wind speed.

For the sake of comparison, we superimpose the robustness index of a reduced stabilizing controller, which comprises a first-order leading and a second-order trailing flap compensator. Note that, although this controller is much leftward in the complex plane, its robustness is significantly lower, indicating that the distance from the imaginary axis is not a good indicator for robustness as it has been suggested in previous studies. Figure 15a demonstrates that, as expected, the robustness index approaches infinity, zero robustness, at flutter instability, 57 m/s for the open-loop system. The performance of the optimal and suboptimal controllers is very similar, and both control approaches achieve good margins up to 67–68 m/s, before the torsional divergence speed. However, system stabilization above torsional divergence has a significant toll on robustness performance. The corresponding root-loci indicate that all closed-loop systems are stable up to 80 m/s; however, achieving good robustness margins is a much more challenging objective.

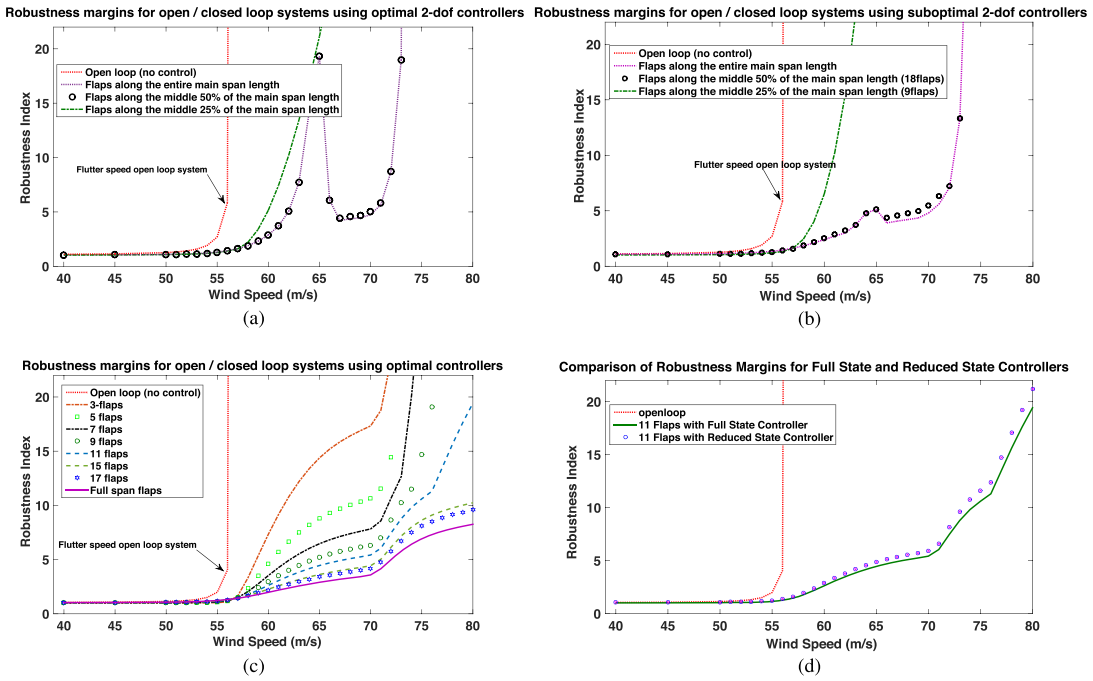

Figure 16. Coprime robustness index of the full FE model as a function of wind speed. (a) Optimal controller designed on the sectional model. (b) 10% suboptimal controller designed on the sectional model. (c) Optimal controller designed on the full FE model. (d) Reduced order optimal controller designed on the full FE model.

DOI: 10.1002/stc

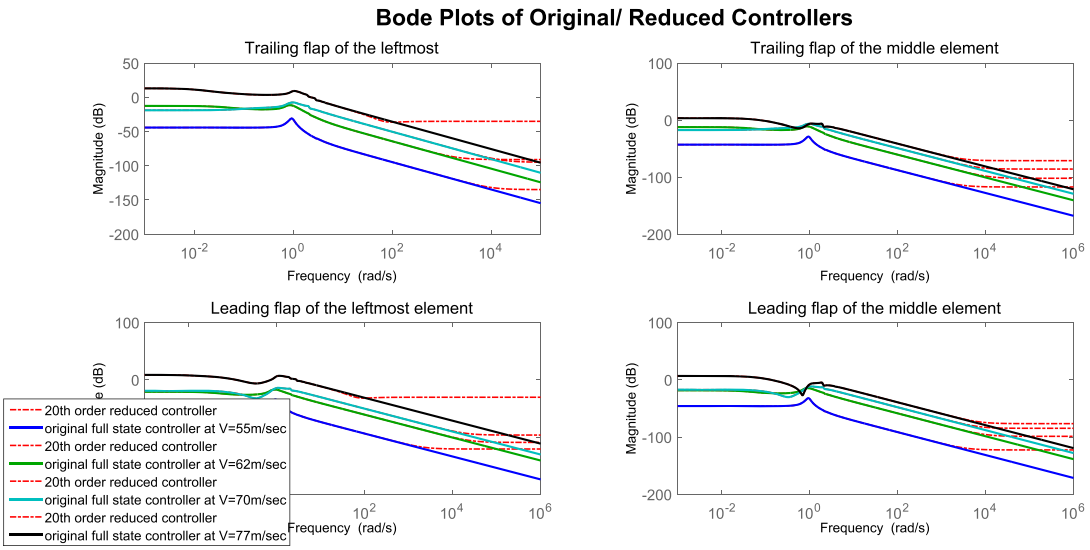

Figure 17. Transfer functions related to four of the 22×11 entries of the control matrix: leftmost leading-edge and trailing-edge flap motion from the pitch of the leftmost element and middle leading-edge and trailing-edge flap motion from the pitch of the middle element.

The optimal controller configuration derived on the section model is then applied to the three-dimensional bridge model. In this case, the controller matrix has a diagonal structure, whereas the same control law is applied to the flaps of each element with each element. The system output is the pitch of the element deck, and the input is the rotation of the flap angles. Figure 16(a) presents the robustness index of the entire structure with flaps along the full length, half-length and quarter-length of the 2400 m main span. It is easily observed that the controller designed on the section model has poor robustness margin when applied to the full bridge. It is evident that the system loses robustness rapidly in the case when 25 % of the span is equipped with winglets, while for longer flap surfaces, an abnormal spike is observed, indicating loss of robustness for certain wind speeds.

Figure 16(b) shows similar graphs, with the difference that the suboptimal controller designed from the sectional model is now applied to the FE model. These figures indicate this strategy yields much smoother robustness margins, without significant loss in performance. In addition, suboptimal controller design is less computationally demanding. Flaps along 50% of the span's length have closely comparable performance with the case of flaps along the 100% of the length. When the wind speed approaches the second flutter instability, 73 m/s, as expected, these controllers are ineffective (robustness index becomes infinite) because the sectional model does not consider those modes.

The final investigation consists in applying the controller design procedure directly on the FE model for different flap lengths located around the midpoint. Figure 16(c) presents the coprime robustness index for those cases. In this modelling example, the main span is modelled using 37 elements (about *65* m width each). It is worth stressing that Figure 16(c) summarizes the best achievable results for enhancing the aeroelastic performance for the chosen model and quantifies the effectiveness of using trailing-edge/leading-edge flaps while retaining good coprime robustness margins. The configuration with 11 flaps, approximately 30 % of the main span length, appears to be a reasonable choice as the aerodynamic instability limit is increased up to 70 m/s with a robustness index $\gamma \approx 5$. Achieving good robustness above the open loop divergence speed and the second flutter mode is very difficult, with a reasonable flap width, even by covering the entire span length with controllable surfaces.

The controller design procedure based on the FE model results in a very high-order controller. For implementation purposes, it is important to implement a reduced-order approximation, preferably with little sacrifice in the performance. There exist several reduction procedures, and for the task at hand [42,43], we perform a truncation operation to the balanced realization of the state space representation of the optimal controller matrix. With this procedure, we are able to reduce substantially (from 400 + to 20 states) the size of the controllers with a negligible loss in performance; Figure 16(d) compares the robustness of the system with full state and reduced-order controller, respectively.

DOI: 10.1002/stc

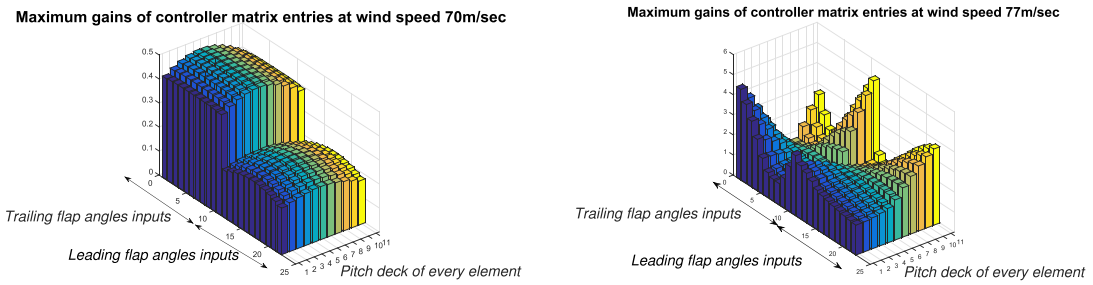

(a) (b)

Figure 18. Maximum magnitudes of the 22×11 transfer functions of the reduced-order controller matrix for wind speeds of (a) 70 m/s and (b) 77 m/s.

In the frame of this design exercise, time simulations at different wind speeds are performed in the case of approximatively 30 % of the main span controlled (11 leading-edge and 11 trailing-edge flaps); consequently, the controller matrix has dimensions 11 by 22. In Figure 17, four of the 242 entries of the matrix are presented, namely, the ones related to the leading-edge and trailing-edge flap motion from the pitch of the leftmost element and those related to the leading-edge and trailing-edge flap motion

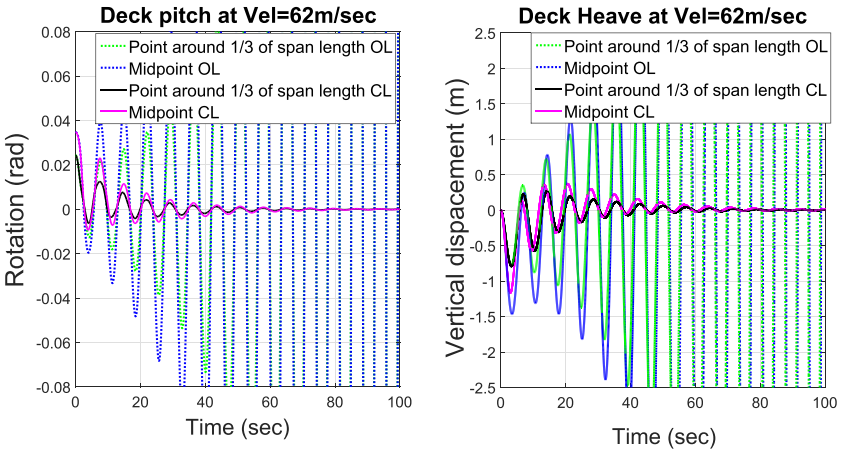

(a)

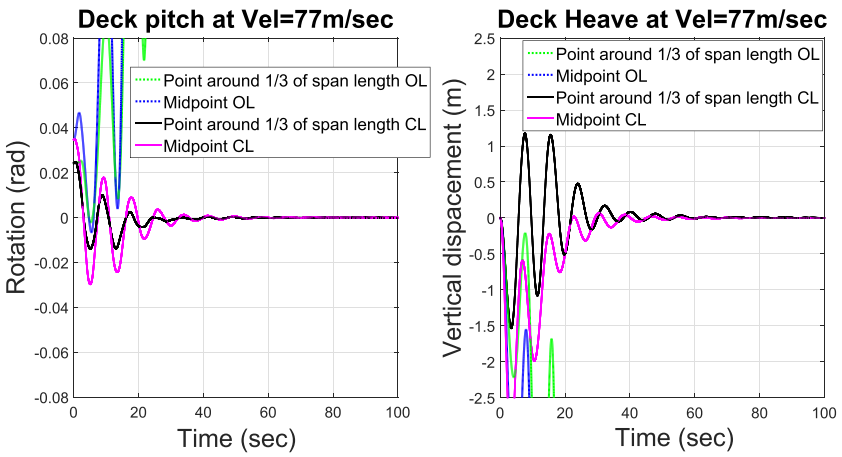

(b)

Figure 19. Deck's pitch and heave transient response at wind speed of (a) 62 m/s and (b) 77 m/s for the open-loop (no controller) and closed-loop system, case 11 flaps around the middle (30% of the whole span), reduced-order controller.

DOI: 10.1002/stc

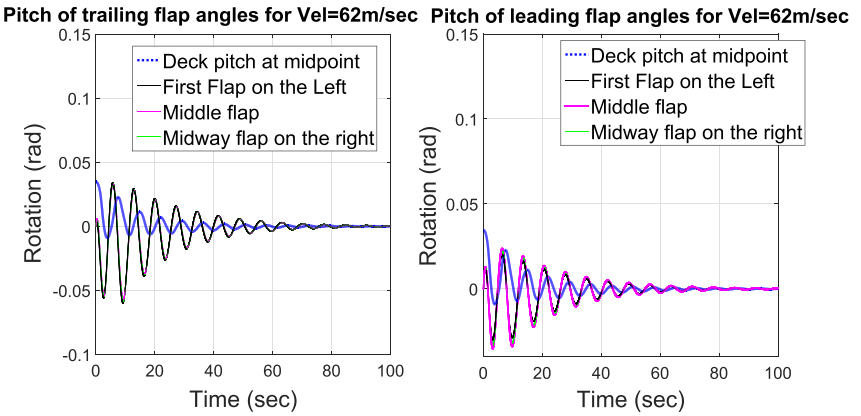

(a)

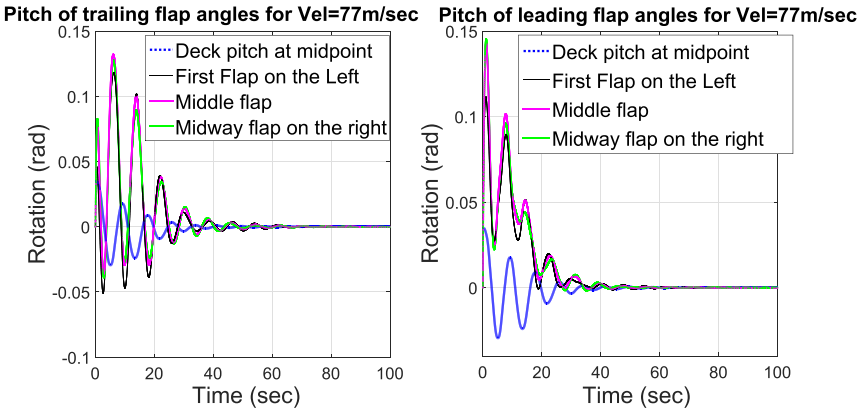

(b)

Figure 20. Flap angles transient response at wind speed of (a) 62 m/s and (b) 77 m/s at three different locations, case 11 flaps around the middle (30% of the whole span), reduced-order controller.

from the pitch of the middle element. Different wind speeds are considered for presentation, namely, 55 m/s (below the first open loop critical flutter speed), 62 m/s (above the first critical flutter speed and below the torsional divergence speed), 70 m/s (above the torsional divergence and below the second flutter speed) and 77 m/s (above the second flutter speed). The 20th state, reduced-order controller is superimposed to the full size controller, showing once again that the two are almost identical in the spectrum of frequencies of interest.

Figure 18 presents the maximum magnitudes of the controller matrix for the two highest wind speeds considered: 70 m/s and 77 m/s. It is interesting to note that at 70 m/s, the flaps in the middle have slightly higher gains than the flap in the edges and that trailing flaps move more than the leading-edge flaps. On the contrary, at 77 m/s, there is an asymmetric distribution of magnitudes due to the flap controller's effort to suppress the first asymmetric torsional mode.

Figure 19 presents the control effectiveness in time domain for suppressing pitching and heaving of the bridge at wind speeds 62 m/s and 77 m/s. The initial condition chosen is that of a sinusoidal twisting/pitch of the main deck with its maximum value at the midpoint of $2^\circ = 0.035$ rad. The transient response of the deck's heave and pitch is presented for two different points (middle and one-third span) for the open-loop system (no flaps active) and the closed-loop system with the 11 flaps around the midpoint (30% of the whole span). When the wind speed is at 62 m/s, the open-loop system diverges in an oscillatory motion because of flutter instability, whereas for a wind speed of 77 m/s, the instability is much more violent as this is a combination of flutter and torsional divergence. It is worth noting that this fictitious simulation is the worst-case example as if we switch on the flap controllers at the chosen wind speed under the given initial condition. In reality, the controllers would already be functioning at lower wind speeds, thus preventing the deck pitch from reaching large values.

DOI: 10.1002/stc

The movement of the flaps with regard to the deck pitch is shown in Figure 20, again for the same wind speeds and initial conditions. Rotations of the leading and trailing flaps at three different locations are presented (middle, leftmost and midway). The time history plots give insight into the flap behaviour for suppressing deck motion. At 62 m/s (and in general, for all wind speeds lower than the second flutter speed), there is a similar behaviour in the movement of the trailing and leading flaps at different locations, showing that potentially, the same control law can be applied for all flaps along the span. On the other hand, this is not the case at 77 m/s. In addition, note that the flap rotations are restricted to less than 10° in the simulation reported. Of course, this depends on the initial condition. However, the transfer function magnitudes show that for wind speeds up to 80 m/s, the rotation of the flaps does not exceed 15°, given a deck pitch of 2°. This is an important observation as larger flap rotations cause flow separations and thin aerofoil theory is no more valid. At this point, it is reminded that our analysis is based on thin airfoil theory, and larger gains for the trailing flap might be required because of flow separation caused by deck bluffness. In [31], it was indeed concluded that a two to three times larger flap deflection is needed than the original controller computation. This finding, however, did not pose a serious issue as the flap angle never exceeded 6° in the experiments.

6. CONCLUSION

The work addressed the issue of suppressing aerodynamic instabilities such as flutter and torsional divergence on long-span suspension bridges using trailing-edge and leading-edge controllable flaps in combination. The initial part of this study dealt with the mathematical formulation for capturing the essential aeroelastic characteristics of suspension bridges using a reduced-size structural model. Classical results from potential flow theory were recast in a form suitable for control analysis and design, implementing therein the transformation of the wing–aileron–tab to the flap–deck–flap configuration, using feedback as well as rational approximation of the circulatory terms, which differentiates this work from previous analyses. The results were compared with previous experimental and analytic studies, finding good agreement. The aeroelastic FE procedure was then extended to implement a rational approximation of the experimentally obtained flutter derivatives. The analysis showed that, for the Great Belt Bridge, the system's aerodynamic behaviour is similar to that predicted by thin aerofoil theory, thus supporting the use of the latter for all subsequent investigations using control surfaces.

In the control part of this work, H_∞ control theory was employed to tackle the robust stabilization of the unstable bridge at high wind velocities. This novel approach successfully quantifies structural and aerodynamic uncertainty and answers questions related to the applicability of a control strategy based on controllable winglets. It was shown that, although the stabilization of the system can be obtained relatively easily, the closed-loop system loses robustness rapidly for wind speeds beyond the open-loop torsional divergence speed. This is an important result that sets a qualitative limit for the performance of all controllers using leading-edge and trailing-edge winglets. However, by fitting the deck with controllable flaps of about 30 % of the main span's total length, it was possible to significantly increase the structure's aeroelastic limits with good robustness margins, that is, the flutter critical speed was raised up to the torsional divergence critical speed. This work demonstrates the feasibility of the proposed aeroelastic control methodology, and although further risk analysis and experimental investigation are needed, the results are encouraging for real bridge applications. The presented high-order active controller implementation also serves as a benchmark for ongoing work on using low-order passive flap controllers, which avoid the use of an external power source and sensors.

ACKNOWLEDGEMENTS

This work was partially funded by the IKY-State Scholarship Foundation by means of the ESPA European fund 2007–2013 and supported by a Marie Curie Intra European Fellowship within the 7th European Community Framework Programme.

DOI: 10.1002/stc

REFERENCES

1. Makoto K. Technology of the Akashi Kaikyo Bridge. *Journal of Structural Control and Health Monitoring* 2004; **11**:75–90.
2. Diana G, Federico C, Alberto Z, Colina A, Bruni S. Aerodynamic design of very long-span suspension bridges. *Long-span and High-rise Structures, IABSE Symposium*, Kobe, 1998; 115–130.
3. Matsumoto M, Mizuno K, Okubo K, Ito Y, Matsumiya M. Flutter instability and recent development in stabilization of structures. *Journal of Wind Engineering and Industrial Aerodynamics* 2007; **95**:888–907.
4. Basu B, Bursi OS, Casciati F, Casciati S, Grosso AED, Domaneschi M, Faravelli L, Szulc JH, Irschik H, Krommer M, Lepidi M, Martelli A, Ozturk B, Pozo F, Pujol G, Rakicevic Z, Rodellar J. A European association for the control of structures joint perspective. recent studies in civil structural control across Europe. *Journal of Structural Control and Health Monitoring* 2014; **21**:1414–1436.
5. Casado CM, Diaz IM, Sebastian J, Poncela AV, Lorenzana A. Implementation of passive and active vibration control on an in-service footbridge. *Journal of Structural Control and Health Monitoring* 2013; **20**:70–87.
6. Ostenfeld KH, Larsen A. Bridge engineering and aerodynamics. *Aerodynamics of Large Bridges, Proceedings of the First International Symposium on Aerodynamics of Large Bridges*, Copenhagen, Denmark, 1992.
7. Wilde K, Fujino Y. Variable-gain control applied to aerodynamic control of bridge deck flutter. *Proceedings of 35th Conference on Decision and Control*, Kobe, Japan, 1996; 682–687.
8. Wilde K, Fujino Y. Aerodynamic control of bridge deck flutter by active surfaces. *Journal of Engineering Mechanics* 1998; **124**(7):718–727.
9. Omenzetter P, Wilde K, Fujino Y. Study of passive deck-flaps flutter control system on full bridge model 1: theory. *Journal of Engineering Mechanics* 2002; **March**:264–279.
10. Omenzetter P, Wilde K, Fujino Y. Study of passive deck-flaps flutter control system on full bridge model 2: results. *Journal of Engineering Mechanics* 2002; **March**:280–286.
11. Hansen HI, Thoft-Christensen P. Active flap control of long suspension bridges. *Journal of Structural Control* 2001; **8** (1):33–82.
12. Li K, Ge YJ, Guo ZW, Zhao L. Theoretical framework of feedback aerodynamic control of flutter oscillation for long-span suspension bridges by the twin-winglet system. *Journal of Wind Engineering and Industrial Aerodynamics* 2015; **145**:166–177.
13. Bakis KN, Massaro M, Williams MS, Limebeer DJN. Aeroelastic control of long span suspension bridges during erection. *IABSE Conference, Elegance in Structures*, Nara, Japan, 2015.
14. Kwon SD, Jung MSS, Chang SP. A new passive aerodynamic control method for bridge flutter. *Journal of Wind Engineering and Industrial Aerodynamics* 2000; **86**:187–2002.
15. Starossek U, Aslan H. Passive control of bridge deck flutter using tuned mass dampers and control surfaces. *7th European Conference on Structural Dynamics*, Southampton, UK, 2008.
16. Astiz MA. Flutter stability of very long span bridges. *Journal of Bridge Engineering* 1998; **3**(3):132–139.
17. Albrecht P, Namini AH, Bosch H. Finite element based flutter analysis of cable suspended bridges. *Journal of Structural Engineering, ASCE* 1992; **118**(6):1509–1526.
18. Starossek U. Prediction of bridge flutter through use of finite elements. *Structural Engineering Review* 1993; **5**(4):301–307.
19. Jones RT. Operational treatment of the nonuniform-lift theory. *NACA Report, TR-667*, 1938.
20. Chen X, Matsumoto M, Kareem A. Aerodynamic coupling effects of flutter and buffeting of bridges. *Journal of Engineering Mechanics* 2000; **126**:17–26.
21. Graham JMR, Limebeer DJN, Zhao X. Aeroelastic control of long-span suspension bridges. *Journal of Applied Mechanics* 2011; **78**:041018–1–041018–12.
22. Limebeer DJN, Graham JMR, Zhao X. Buffet suppression in long-span suspension bridges. *Annual Reviews in Control* 2011; **35**:235–246.
23. Abdel-Ghaffar AM. Free lateral vibrations of suspension bridges. *Journal of Structural Division ASCE* 1978; **104** (ST3):503–525.
24. Abdel-Ghaffar AM. Free torsional vibrations of suspension bridges. *Journal of Structural Division ASCE* 1979; **105** (ST4):767–788.
25. Abdel-Ghaffar AM. Free vertical vibrations of suspension bridges. *Journal of Structural Division ASCE* 1980; **105** (ST10):2053–2076.
26. Irvine HM. Studies in the statics and dynamics of simple cable systems. *Technical Report*, California Institute of Technology, 1974.
27. Theodorsen T. General theory of aerodynamic instability and the mechanisms of flutter. *NACA Report, TR-496*, 1934.
28. Jain A, Jones NP, Scanlan RH. Coupled flutter and buffeting analysis of long-span bridges. *Journal of Structural Engineering, ASCE* 1996; **122**:716–725.
29. Roger KL. Airplane Math Modelling Methods for Active Control Design. AGAPO-CP-228: New York, 1997.
30. Bisplinghoff RL, Ashley H, Halfman RL. Aeroelasticity. Dover Publications: New York, 1996.
31. Gouder K, Zhao X, Limebeer DJN, Graham JMR. Experimental aerodynamic control of a long-span suspension bridge section using leading and trailing edge control surfaces. *IEEE Transactions on Control System Technology* 2015; **PP**:1–13. doi: 10.1109/TCST.2015.2501346.
32. Larsen A. Aerodynamic aspects of the final design of the 1624 m suspension bridge across the Great Belt. *Journal of Wind Engineering and Industrial Aerodynamics* 1993; **48**:261–285.
33. Jurado JA, Hermandez S, Nieto F, Mosquera A. Bridge Aeroelasticity: Sensitivity Analysis and Optimum Design. WIT Press: Southampton, Boston, 2011.
34. Cobo D. An analysis of wind stability. Improvements to the response of suspension bridges. *Tesis doctoral de la Universitat de Catalunya*, 1998.
35. Lopes GBR, Silva RS. Time domain modelling and bridge deck flutter and applications. *Mecanica Computational* 2010; **14**:529–5553.
36. Scanlan RH, Tomko JJ. Airfoil and bridge deck flutter derivatives. *Journal of Engineering Mechanics* 1971; **97** (6):1717–1737.

DOI: 10.1002/stc

37. Scanlan RH. Observations on low-speed aeroelasticity. *Journal of Engineering Mechanics* 2012; **128**:1254–1258.
38. Scanlan RH. Problematics in formulation of wind-force model for bridge deck. *Journal of Engineering Mechanics* 1993; **119**:1353–1375.
39. Starossek U, Aslan H, Thiesemann L. Experimental and numerical identification of flutter derivatives for nine bridge deck sections. *Wind and Structures* 2009; **12**(6):519–540.
40. Theodorsen T, Garrick IE. Nonstationary flow about a wing–aileron–tab combination including aerodynamic balance. *NACA Report, TR-736*, 1942.
41. Tuanjie L, Yujuan M. Robust vibration control of flexible tensegrity structure via μ synthesis. *Journal of Structural Control and Health Monitoring* 2011; **20**:173–186.
42. Green M, Limebeer DJN. Linear Robust Control. Prentice Hall: Englewood Cliffs, NJ, 1995.
43. Skogestad S, Postlethwaite I. Multivariable Feedback Control: Analysis and Design (2nd edn). Wiley: Chichester; New York; Brisbane; Toronto; Singapore, 2006.

DOI: 10.1002/stc